

9 Graphical modelling of dynamic relationships in multivariate time series

Michael Eichler

Institut für Angewandte Mathematik
Universität Heidelberg
Germany

SUMMARY

The identification and analysis of interactions among multiple simultaneously recorded time series is an important problem in many scientific areas. Of particular interest are directed interactions that describe the dynamics of the systems and thus help to determine the causal driving mechanisms of the underlying system. The dynamic relationships among multiple series intuitively can be visualized by a path diagram (or graph), in which the variables are represented by vertices or nodes, and directed edges between the vertices indicate the dynamic or causal influences among the variables. In this chapter, we review recent results on the properties of such graphical representation, which show that path diagrams provide an ideal basis for discussing and investigating causal relationships in multivariate time series. The key role in this graphical approach is played by so-called global Markov properties, which provide graphical conditions for the (in-)dependencies that may be observed if only subprocesses instead of the full process are considered. Such considerations are, for example, central for the discussion of systems that may contain latent variables. The empirical analysis of dynamic interactions is commonly based on the concept of Granger causality. While this concept is well understood in the time domain, the time series of interest often are characterized in terms of their spectral properties. Therefore, particular emphasis will be given to the the frequency domain interpretation of Granger causality and the graphical concepts discussed in this chapter.

9.1 Introduction

The analysis of the interrelationships among multiple simultaneously recorded time series is an important problem in a variety of fields such as economics, engineering, the physical and the life sciences. Of particular interest are the dynamic relationships over time among the series, which help to determine the causal driving mechanisms of the underlying system. In neuroscience, for instance, signals reflecting neural activity such as electroencephalographic (EEG) or local field potentials (LFP) recordings have been used to learn patterns of interactions between brain areas that are activated during certain tasks and to improve thus our understanding of neural processing of information (e.g., [1, 2]).

The most commonly used approach for describing and inferring dynamic or causal relationships in multivariate time series is based on vector autoregressive models and the concept

of Granger causality [3]. This probabilistic concept of causality is based on the common sense perception that causes always precede their effects in time: if one time series causes another series, knowledge of the former series should help to predict future values of the latter series after influences of other variables have been taken into account. Since the concept does not rely on an a priori specification of a causal model, it is particularly suited for empirical investigations of cause-effect relationships; being basically a measure of association, however, it can lead to so-called spurious causalities if important relevant variables are not included in the analysis (e.g., [4]).

An intuitive approach to summarize the dynamic relationships in complex systems is to represent them in a graph, in which a set of vertices or nodes represents the variables and directed edges between the vertices indicate the dynamic or causal influences among the variables. The graphical representation of causal structures goes back to Wright [5, 6], who introduced path diagrams for the discussion of linear structural equation systems. More recently, graphs have been used to visualize and analyse the dependencies among variables in multivariate data; for an introduction to the theory of graphical models we refer to the monographs of Whittaker [7], Cox and Wermuth [8], Lauritzen [9], and Edwards [10]. These theoretical advances and the introduction of Bayesian networks [11, 12] have stimulated new interest in graphical representations of causal structures and have led to the developments of concepts for a graph-theoretic analysis of causality (e.g., [13, 14, 15, 16]).

For the analysis of the dynamic relationships in multivariate time series, Eichler [17, 18, 19] has introduced path diagrams that visualize the autoregressive structure of weakly stationary processes and, thus, encode the Granger-causal relationships among the variables of these processes. These graphs provide an ideal basis for discussing and investigating causal relationships in multivariate time series since, on the one hand, their Markov interpretation allows conclusions on which dependencies may be observed in arbitrary subprocesses and, on the other hand, they have a natural causal interpretation if the observed process comprises all relevant variables. Thus, the graphs can be used, for instance, to examine whether the observed (in-)dependencies in a vector time series are consistent with the theoretically predicted (in-)dependencies derived from a hypothesized causal structure that possibly contains latent variables.

In this chapter we review the basic concepts for this graphical approach: Granger causality, path diagrams for vector autoregressions and their Markov properties, and statistical inference for such graphs. Since in many applications, especially in neuroscience, the time series of interest are characterized in terms of their spectral properties, particular emphasis will be given to the frequency domain interpretation of Granger causality and the related graphical representations. We find that causal modelling in the frequency domain leads to linear structural equation systems for the frequency components of the process, whose structure is visualized by the path diagram associated with the autoregressive representation of the process.

9.2 Granger causality in multivariate time series

The concept of Granger causality is a fundamental tool for the empirical investigation of dynamic interactions in multivariate time series. This probabilistic concept of causality is based on the common sense conception that causes always precede their effects. Thus an

event taking place in the future cannot cause another event in the past or present. This temporal ordering implies that the past and present values of a series X that influences another series Y should help to predict future values of this latter series Y . Furthermore, the improvement in the prediction of future values of Y should persist after any other relevant information for the prediction has been exploited. Suppose that the vector time series \mathbf{Z} comprises all variables that might affect the dependence between X and Y such as confounding variables. Then we say that a series X Granger-causes another series Y with respect to the information given by the series (X, Y, \mathbf{Z}) if the value of $Y(t+1)$ can be better predicted by using the entire information available at time t than by using the same information apart from the past and present values of X . Here, ‘better’ means a smaller variance of forecast error.

Because of the temporal ordering, it is clear that Granger causality can only capture functional relationships for which cause and effect are sufficiently separated in time. To describe causal dependencies between variables at the same time point, Granger [3] proposed the notion of ‘instantaneous causality’. In general, it is not possible to attribute a unique direction to such ‘instantaneous causalities’ and we therefore will only speak of contemporaneous dependencies.

In practice, the use of Granger causality mostly has been restricted to the investigation of linear relationships. This notion of linear Granger causality is closely related to the autoregressive representation of a weakly stationary process.

9.2.1 Granger causality and vector autoregressions

Let $\mathbf{X}_V = \{\mathbf{X}_V(t), t \in \mathbb{Z}\}$ with $\mathbf{X}_V(t) = (X_v(t), v \in V)'$ be a weakly stationary vector time series with mean zero and covariances $\mathbf{c}(u) = \mathbb{E}\mathbf{X}_V(t)\mathbf{X}_V(t-u)'$. Throughout this chapter, we assume that the spectral density matrix

$$\mathbf{f}(\lambda) = \frac{1}{2\pi} \sum_{u \in \mathbb{Z}} \mathbf{c}(u) e^{-i\lambda u}$$

exists and that all its eigenvalues are bounded and bounded away from zero uniformly for all frequencies $\lambda \in [-\pi, \pi]$. Under these assumptions, the process \mathbf{X}_V has an autoregressive representation of the form

$$\mathbf{X}_V(t) = \sum_{u \in \mathbb{N}} \mathbf{a}(u) \mathbf{X}_V(t-u) + \boldsymbol{\varepsilon}_V(t), \quad (9.1)$$

where $\mathbf{a}(u)$ is a square summable sequence of $V \times V$ matrices and $\{\boldsymbol{\varepsilon}_V(t)\}$ is a white noise process with mean zero and non-singular covariance matrix $\boldsymbol{\Sigma}$. From the equation for $X_i(t)$, we obtain for the mean square prediction error when $X_i(t)$ is predicted from the past values of \mathbf{X}_V

$$\text{var}(X_i(t) | \overline{\mathbf{X}}_V(t-1)) = \text{var}(\varepsilon_i(t)) = \sigma_{ii}. \quad (9.2)$$

Here, $\overline{\mathbf{X}}_V(t-1) = \{\mathbf{X}_V(t-u), u \in \mathbb{N}\}$ denotes the past values of \mathbf{X}_V at time t and conditional variance is taken to be the variance about the linear projection.

Similarly, if we consider the subprocess $\mathbf{X}_{-j} = \mathbf{X}_{V \setminus \{j\}}$ consisting of all components but X_j , it follows from the above assumptions on the spectral matrix that \mathbf{X}_{-j} has an autoregressive representation

$$\mathbf{X}_{-j}(t) = \sum_{u \in \mathbb{N}} \tilde{\mathbf{a}}(u) \mathbf{X}_{-j}(t-u) + \boldsymbol{\eta}_{-j}(t), \quad (9.3)$$

where $\{\boldsymbol{\eta}_{-j}(t)\}$ is a white noise process with mean zero and covariance matrix $\tilde{\boldsymbol{\Sigma}}$. Thus, the mean square prediction error for predicting $X_i(t)$ from the past values of \mathbf{X}_{-j} is given by

$$\text{var}(X_i(t) | \overline{\mathbf{X}}_{-j}(t-1)) = \text{var}(\eta_i(t)) = \tilde{\sigma}_{ii}. \quad (9.4)$$

In general, the mean square prediction error in (9.4) will be larger than that in (9.2), and the two variances will be equal if and only if the best linear predictor of $X_i(t)$ based on the full past $\overline{\mathbf{X}}_V(t-1)$ does not depend on the past values of X_j . This leads to the following definition of Granger noncausality, which we state more generally for vector subprocesses \mathbf{X}_I and \mathbf{X}_J . Here, $|\mathbf{A}|$ denotes the determinant of a square matrix \mathbf{A} .

Definition 9.2.1. Let I and J be two disjoint subsets of V . Then \mathbf{X}_J is *Granger-noncausal* for \mathbf{X}_I with respect to \mathbf{X}_V if the following two equivalent conditions hold:

- (i) $|\text{var}(\mathbf{X}_I(t) | \overline{\mathbf{X}}_{V \setminus J}(t-1))| = |\text{var}(\mathbf{X}_I(t) | \overline{\mathbf{X}}_V(t-1))|$;
- (ii) $\mathbf{a}_{IJ}(u) = 0$ for all $u \in \mathbb{N}$.

Furthermore, if $\boldsymbol{\Sigma}_{IJ} = 0$, we say that \mathbf{X}_I and \mathbf{X}_J are *contemporaneously uncorrelated* with respect to \mathbf{X}_V .

In other words, the variables $X_I(t)$ and $X_J(t)$ are contemporaneously uncorrelated with respect to \mathbf{X}_V if they are uncorrelated after removing the linear effects of $\overline{\mathbf{X}}_V(t-1)$. We note that the autoregressive representations describe only linear relationships among the variables and thus, strictly speaking, relate to linear Granger noncausality. In the sequel, we will use the term Granger noncausality in this restricted meaning.

In practice, tests for Granger noncausality are mostly based on condition (ii) as it is formulated only in terms of the autoregressive coefficients in the full model and, thus, does not require fitting of multiple models (e.g., [20, 4, 21, 22]); the measure for conditional linear feedback proposed by Geweke [23], however, is based on condition (i).

From the definition of Granger noncausality in terms of the autoregressive parameters, it is clear that the notion of Granger noncausality depends on the multivariate time series \mathbf{X}_V available for the analysis. If we consider only a subprocess $\mathbf{X}_{V'}$ with $V' \subseteq V$ instead of the full process \mathbf{X}_V , the vector time series $\mathbf{X}_{V'}$ has again an autoregressive representation

$$\mathbf{X}_{V'}(t) = \sum_{u \in \mathbb{N}} \tilde{\mathbf{a}}(u) \mathbf{X}_{V'}(t-u) + \tilde{\boldsymbol{\varepsilon}}_{V'}(t),$$

but the coefficients $\tilde{\mathbf{a}}(u)$ in general will differ from the coefficients $\mathbf{a}_{V'V'}(u)$ in the representation (9.1). To illustrate this dependence on the set of selected variables, we consider the four-dimensional vector autoregressive process \mathbf{X}_V with components

$$\begin{aligned} X_1(t) &= \alpha X_4(t-2) + \varepsilon_1(t), \\ X_2(t) &= \beta X_4(t-1) + \gamma X_3(t-1) + \varepsilon_2(t), \\ X_3(t) &= \varepsilon_3(t), \\ X_4(t) &= \varepsilon_4(t), \end{aligned} \quad (9.5)$$

where $\varepsilon_v(t)$, $v = 1, \dots, 4$ are independent and identically normally distributed with mean zero and variance σ^2 . From (9.5), we find that, for example, X_3 Granger-causes X_2 with respect to \mathbf{X}_V , but not X_1 or X_4 . However, if we consider only the three-dimensional subprocess $\mathbf{X}_{\{1,2,3\}}$, simple calculations show that $\mathbf{X}_{\{1,2,3\}}$ is given by

$$\begin{aligned} X_1(t) &= \frac{\alpha\beta}{1+\beta^2} X_2(t-1) - \frac{\alpha\beta\gamma}{1+\beta^2} X_3(t-2) + \tilde{\varepsilon}_1(t), \\ X_2(t) &= \gamma X_3(t-1) + \tilde{\varepsilon}_2(t), \\ X_3(t) &= \tilde{\varepsilon}_3(t), \end{aligned} \tag{9.6}$$

where $\tilde{\varepsilon}_3(t) = \varepsilon_3(t)$, $\tilde{\varepsilon}_2(t) = \varepsilon_2(t) + \beta X_4(t-1)$, and

$$\tilde{\varepsilon}_1(t) = \varepsilon_1(t) - \frac{\alpha\beta}{1+\beta^2} \varepsilon_2(t-1) + \frac{\alpha}{1+\beta^2} X_4(t-2).$$

From this representation, it follows that X_3 Granger-causes not only X_2 but also X_1 with respect to $\mathbf{X}_{\{1,2,3\}}$. In contrast, if we restrict the information further and consider only the bivariate subprocess $\mathbf{X}_{\{1,3\}}$, we obtain from (9.6) that the two components X_1 and X_3 are two uncorrelated white noise processes; in particular, this implies that X_3 is Granger-noncausal for X_1 with respect to $\mathbf{X}_{\{1,3\}}$.

9.2.2 Granger causality in the frequency domain

In many applications, the time series of interest are characterized in terms of their frequency properties; typical examples can be found in chapters 10 and 11. It is therefore important to examine the relationships among multiple time series also in the frequency domain. The frequency domain analysis of weakly stationary vector time series \mathbf{X}_V is based on the spectral representation of \mathbf{X}_V , which is given by

$$\mathbf{X}_V(t) = \int_{-\pi}^{\pi} e^{i\lambda t} d\mathbf{Z}_{\mathbf{X}_V}(\lambda), \tag{9.7}$$

where $d\mathbf{Z}_{\mathbf{X}_V}(\lambda)$ is a random process on $[-\pi, \pi]$ that takes values in \mathbb{C}^V and has mean zero and orthogonal increments (e.g., [24]). In this representation, the complex-valued random increments $dZ_{X_i}(\lambda)$ indicate the frequency components of the time series X_i at frequency λ . The increments are related to the spectral density matrix of \mathbf{X}_V by

$$\mathbb{E}(d\mathbf{Z}_{\mathbf{X}_V}(\lambda)d\mathbf{Z}_{\mathbf{X}_V}(\mu)') = \mathbf{f}(\lambda)\delta(\lambda - \mu)d\lambda d\mu,$$

where $\delta(u)$ is the Dirac delta function. In other words, the spectral density matrix $\mathbf{f}(\lambda)$ can be viewed as the covariance matrix of the frequency components of \mathbf{X}_V at frequency λ . Similarly, let

$$\varepsilon_V(t) = \int_{-\pi}^{\pi} e^{i\lambda t} d\mathbf{Z}_{\varepsilon_V}(\lambda)$$

be the spectral representation of the error process $\varepsilon_V = \{\varepsilon_V(t)\}$ in the autoregressive representation of \mathbf{X}_V in (9.1). Since ε_V is a white noise process with covariance matrix Σ , the

increments $d\mathbf{Z}_{\varepsilon_V}(\lambda)$ satisfy

$$\mathbb{E}(d\mathbf{Z}_{\varepsilon_V}(\lambda)d\mathbf{Z}_{\varepsilon_V}(\mu)') = \Sigma \delta(\lambda - \mu) d\lambda d\mu.$$

The autoregressive representation implies that the frequency components of the processes \mathbf{X}_V and ε_V are related by the linear equation system

$$d\mathbf{Z}_{\mathbf{X}_V}(\lambda) = \mathbf{A}(\lambda) d\mathbf{Z}_{\mathbf{X}_V}(\lambda) + d\mathbf{Z}_{\varepsilon_V}(\lambda), \quad (9.8)$$

where

$$\mathbf{A}(\lambda) = \sum_{u \in \mathbb{N}} \mathbf{a}(u) e^{-i\lambda u} \quad (9.9)$$

is the Fourier transform of the autoregressive coefficients $\mathbf{a}(u)$. The coefficient $A_{ij}(\lambda)$ vanishes uniformly for all $\lambda \in [-\pi, \pi]$ if and only if X_j is Granger-noncausal for X_i with respect to \mathbf{X}_V . This suggests that the linear equation system (9.8) reflects the causal pathways by which the frequency components influence each other. More precisely, the complex-valued coefficient $A_{ij}(\lambda)$ indicates how a change in the frequency component of the series X_j affects the frequency component of X_i if all other components are held fixed, that is, $A_{ij}(\lambda)$ measures the direct causal effect of X_j on X_i at frequency λ .

As a coefficient in a linear equation system, $A_{ij}(\lambda)$ is not scale invariant, which makes it difficult to assess the strength of a directed relationship. Baccala and Sameshima [25, 26] used a factorization of the partial spectral coherence to derive a normalized frequency domain measure for Granger causality, which they called *partial directed coherence* (PDC). The PDC from X_j to X_i is defined as

$$\pi_{ij}(\lambda) = \frac{\bar{A}_{ij}(\lambda)}{\sqrt{\sum_{k \in V} |\bar{A}_{kj}(\lambda)|^2}},$$

where $\bar{\mathbf{A}}(\lambda) = \mathbf{I} - \mathbf{A}(\lambda)$ and \mathbf{I} is the identity matrix. With this normalization, the PDC indicates the relative strength of the effect of X_j on X_i as compared to the strength of the effect of X_j on the other variables. Thus, partial directed coherence ranks the relative interaction strengths with respect to a given signal source. We note that other normalizations are possible; in section 9.5, we propose an alternative rescaling based on an asymptotic significance level.

Linear equation systems have been widely used in economics and in the social sciences for simultaneously representing causal and statistical hypotheses relating a set of variables (e.g., [27, 28, 29]). In general, the structure of such systems is not uniquely determined by the distribution of the variables and, thus, cannot be determined empirically from data, but, on the contrary, must be determined from prior knowledge of the causal relations. In contrast, the coefficients in the above systems (9.9) are completely specified by the unique autoregressive representation of the process \mathbf{X}_V and the implied requirements that $\mathbf{A}(\lambda)$ must be of the form (9.9) and that the covariance matrix of the error term $d\mathbf{Z}_{\varepsilon_V}(\lambda)$ does not depend on the frequency λ .

Finally, we note that such causal interpretations should be treated with caution since they rely on the assumption that all relevant information has been included. The omission of important variables can lead to so-called spurious causalities, which invalidate the causal interpretation of empirically determined Granger-causal relationships among the variables.

9.2.3 Bivariate Granger causality

Although Granger [3, 30] always stressed the need to include all relevant information in an analysis to avoid spurious causalities, much of the literature on Granger causality has been concerned with the analysis of relationships between two time series or two vector time series (see, e.g., [31, 32, 33, 34]). As a consequence, relationships among multiple time series are still quite frequently investigated using bivariate Granger causality, that is, analysing pairs of time series separately (see, e.g., [35, 36, 37, 38]). For a better understanding of this bivariate approach and its relation to a full multivariate analysis based on multivariate Granger causality, we will discuss in the sequel also the use of bivariate Granger causality for describing directed relationships among multiple time series.

Suppose that \mathbf{X}_V is a weakly stationary process of the form (9.1). Then for $i, j \in V$ the bivariate subprocess $\mathbf{X}_{\{i,j\}}$ is again a weakly stationary process and has an autoregressive representation

$$\begin{aligned} X_i(t) &= \sum_{u \in \mathbb{N}} \tilde{a}_{ii}(u) X_i(t-u) + \sum_{u \in \mathbb{N}} \tilde{a}_{ij}(u) X_j(t-u) + \tilde{\varepsilon}_i(t), \\ X_j(t) &= \sum_{u \in \mathbb{N}} \tilde{a}_{ji}(u) X_i(t-u) + \sum_{u \in \mathbb{N}} \tilde{a}_{jj}(u) X_j(t-u) + \tilde{\varepsilon}_j(t), \end{aligned} \quad (9.10)$$

where $\tilde{\varepsilon}(t) = (\tilde{\varepsilon}_i(t), \tilde{\varepsilon}_j(t))'$ is a white noise process with covariance matrix $\tilde{\Sigma}$. From this representation, it follows that X_j is bivariate Granger-causal for X_i if and only if the coefficients $\tilde{a}_{ij}(u)$ are zero for all lags $u \in \mathbb{N}$. Similarly, X_i and X_j are bivariate contemporaneously uncorrelated if $\tilde{\sigma}_{ij} = 0$.

9.3 Graphical representations of Granger causality

The causal relationships among the variables in complex multivariate systems are often visually summarized by graphs in which the nodes or vertices represent the variables and directed edges between the vertices indicate causal influences among the variables. In this section, we formally define such graphs for representing the multivariate or the bivariate Granger-causal relationships in multivariate time series; the properties of these graphs will then be discussed in Section 9.4.

9.3.1 Path diagrams for multivariate time series

Intuitively, the Granger-causal relationships in a weakly stationary vector time series \mathbf{X}_V can be encoded and visualized by a path diagram in which the vertices $v \in V$ represent the components X_v of the process and directed edges (\longrightarrow) between the vertices indicate Granger-causal influences. To obtain a complete description of the dependence structure of \mathbf{X}_V , we additionally include undirected edges ($---$) to depict contemporaneous correlations between the components of \mathbf{X}_V . Since the Granger-causal relationships of \mathbf{X}_V are determined by the autoregressive representation of \mathbf{X}_V , we obtain the following definition of path diagrams associated with vector autoregressive processes [19, 39].

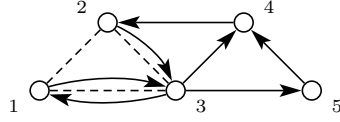


Figure 9.1: Path diagram associated with a five-dimensional VAR(1) process that satisfies the parameter constraints in (9.11) and (9.12).

Definition 9.3.1. Let \mathbf{X}_V be a weakly stationary time series with autoregressive representation (9.1). Then the *path diagram associated with \mathbf{X}_V* is a graph $G = (V, E)$ with vertex set V and edge set E such that for $i, j \in V$ with $i \neq j$

- (i) $j \longrightarrow i \notin E \Leftrightarrow a_{ij}(u) = 0 \quad \text{for } u \in \mathbb{N};$
- (ii) $j \text{ --- } i \notin E \Leftrightarrow \sigma_{ij} = 0.$

In other words, the path diagram G contains a directed edge $j \longrightarrow i$ if and only if X_j Granger-causes X_i with respect to the full series \mathbf{X}_V ; similarly, an undirected edge $i \text{ --- } j$ is present in the path diagram if and only if X_i and X_j are contemporaneously correlated with respect to \mathbf{X}_V . For this reason, such path diagrams have also been called *Granger causality graphs* [17, 40].

The path diagram associated with a process \mathbf{X}_V has also a natural interpretation in terms of the frequency components $d\mathbf{Z}_{\mathbf{X}_V}(\lambda)$ of \mathbf{X}_V . As we have seen in Section 9.2.2 that the autoregressive representation of \mathbf{X}_V corresponds to the linear equation systems

$$d\mathbf{Z}_{\mathbf{X}_V}(\lambda) = \mathbf{A}(\lambda) d\mathbf{Z}_{\mathbf{X}_V}(\lambda) + d\mathbf{Z}_{\varepsilon_V}(\lambda),$$

where the error component $d\mathbf{Z}_{\varepsilon_V}(\lambda)$ has basically covariance matrix Σ . It follows that the path diagram G associated with \mathbf{X}_V can also be viewed as the path diagram of the above linear equation systems¹ for all frequencies λ , and its edges equivalently are determined by the conditions

- (i) $j \longrightarrow i \notin E \Leftrightarrow A_{ij}(\lambda) = 0 \quad \text{for } \lambda \in [-\pi, \pi];$
- (ii) $j \text{ --- } i \notin E \Leftrightarrow \sigma_{ij} = 0.$

We note that two vertices in a path diagram may be connected by up to three edges. As an example, we consider the five-dimensional vector autoregressive process

$$\mathbf{X}(t) = \mathbf{a} \mathbf{X}(t-1) + \varepsilon(t), \quad \text{var}(\varepsilon(t)) = \Sigma$$

¹In path diagrams for structural equation systems, correlated errors commonly are represented by bi-directed edges (\longleftrightarrow) instead of dashed lines (---). Since in our approach directions are associated with temporal ordering, we prefer (dashed) undirected edges to indicate correlation between the error variables. Dashed edges with a similar connotation are used for covariance graphs (e.g., [8]), whereas undirected edges --- are commonly associated with nonzero entries in the inverse of the variance matrix (e.g., [9]).

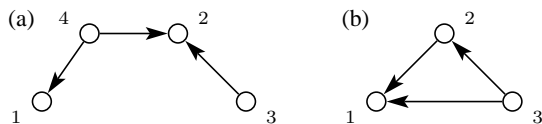


Figure 9.2: Path diagrams associated with (a) four-dimensional process \mathbf{X}_V given by (9.5) and with (b) three-dimensional subprocess $\mathbf{X}_{\{1,2,3\}}$.

with coefficient matrix

$$\mathbf{a} = \begin{pmatrix} a_{11} & 0 & a_{13} & 0 & 0 \\ 0 & a_{22} & 0 & a_{24} & 0 \\ a_{31} & a_{32} & a_{33} & 0 & 0 \\ 0 & 0 & a_{43} & a_{44} & a_{45} \\ 0 & 0 & a_{53} & 0 & a_{55} \end{pmatrix} \quad (9.11)$$

and covariance matrix

$$\Sigma = \begin{pmatrix} \sigma_{11} & \sigma_{12} & \sigma_{13} & 0 & 0 \\ \sigma_{21} & \sigma_{22} & \sigma_{23} & 0 & 0 \\ \sigma_{31} & \sigma_{32} & \sigma_{33} & 0 & 0 \\ 0 & 0 & 0 & \sigma_{44} & 0 \\ 0 & 0 & 0 & 0 & \sigma_{55} \end{pmatrix}. \quad (9.12)$$

The autoregressive structure of \mathbf{X}_V is visualized by the associated path diagram shown in Figure 9.1. The diagram indicates, for example, that there is a feedback loop between variables X_1 and X_3 , or that X_1 affects X_4 indirectly with X_3 as mediating variable.

From our discussion in Section 9.2.1, it is clear that the path diagram depends on the set of variables included in the process \mathbf{X}_V . To illustrate this dependence, let us again consider the four-dimensional process in (9.5). Its associated path diagram is depicted in Figure 9.2(a), which, for example, shows that X_3 is Granger-noncausal for X_1 with respect to \mathbf{X}_V . In contrast, if we consider only variables X_1 , X_2 , and X_3 , the corresponding autoregressive representation in (9.6) yields the path diagram in Figure 9.2(b); in this graph, there is a directed edge from vertex 3 to vertex 1, which implies that X_3 Granger-causes X_1 with respect to the subprocess $\mathbf{X}_{\{1,2,3\}}$.

We note that more detailed graphical descriptions of the dependencies among the components of \mathbf{X}_V are possible by representing each variable $X_v(t)$ for all time points t by a separate node (see, e.g., [41, 42, 40]). However, identification of such graphs easily becomes infeasible due to the large number of possible edges. Moreover, such a level of detail is not always wanted; in particular, graphs of this type have no direct interpretation in terms of the frequency components of the process.

9.3.2 Bivariate Granger causality graphs

When the directed relationships in a vector time series \mathbf{X}_V are described in terms of bivariate Granger causality, the results of such bivariate analyses again can be graphically represented

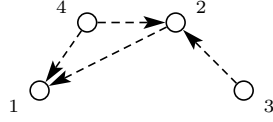


Figure 9.3: Bivariate Granger causality graph associated with four-dimensional process \mathbf{X}_V given by (9.5).

by a path diagram. In these graphs, bivariate Granger-causal relationships will be indicated by dashed directed edges ($-\!\!\rightarrow$) in order to distinguish these edges from the directed edges in multivariate path diagrams, which represent Granger causal influences with respect to the full multivariate process \mathbf{X}_V . This leads to the following definition of *bivariate path diagrams* or *bivariate Granger causality graphs*, which visualizes the bivariate connectivities in vector time series.

Definition 9.3.2. Let \mathbf{X}_V be a weakly stationary time series of the form (9.1). Then the *bivariate path diagram associated with \mathbf{X}_V* is a graph $G = (V, E)$ with vertex set V and edge set E such that for all $i, j \in V$ with $i \neq j$

- (i) $j \rightarrow i \notin E \Leftrightarrow \tilde{\alpha}_{ij}(u) = 0 \quad \text{for } u \in \mathbb{N},$
- (ii) $j \dashrightarrow i \notin E \Leftrightarrow \tilde{\sigma}_{ij} = 0,$

where $\tilde{\alpha}_{ij}(u)$, $u \in \mathbb{N}$ and $\tilde{\sigma}_{ij}$ are the parameters in the autoregressive representation (9.10) of the bivariate subprocess $\mathbf{X}_{\{i,j\}}$.

From the above definition, it is clear that, for any subprocess \mathbf{X}_S of \mathbf{X}_V , the bivariate Granger causality graph of \mathbf{X}_S is given by the subgraph G_S that is obtained from the bivariate causality graph G by removing all vertices that are not in S and all edges—directed or undirected—that do not have both endpoints in S .

As an example, we consider again the four-dimensional process in (9.5). For the bivariate Granger causality graph, we have to determine the bivariate autoregressive representations for all pairs X_i and X_j . Simple calculations show, for example, that $\mathbf{X}_{\{1,2\}}$ is given by

$$\begin{aligned} X_1(t) &= \frac{\alpha\beta}{1 + \beta^2 + \gamma^2} X_2(t-1) + \tilde{\varepsilon}_1(t), \\ X_2(t) &= \tilde{\varepsilon}_2(t). \end{aligned}$$

Furthermore, we have already shown in Section 9.2.1 that the components X_1 and X_3 are completely uncorrelated in a bivariate analysis. Evaluating similarly the autoregressive representations for all other bivariate subprocesses, we obtain the bivariate path diagram in Figure 9.3 as a visualization of the bivariate Granger causal relationships among the variables. In this graph, the directed edge $2 \rightarrow 1$ suggests a causal influence of X_2 on X_1 . Comparison with the corresponding multivariate path diagram in Figure 9.2(a) shows that this “causal influence” is spurious as it is only induced by the common influence from variable X_4 .

In general, the relationship between the two notions of multivariate and bivariate Granger causality is more complicated than in this simple example, and, in most cases, an analytic derivation of the bivariate representation would be very difficult to obtain. In the following

section, we discuss graphical conditions that allow drawing conclusions about one graph from the other.

9.4 Markov interpretation of path diagrams

The edges in the path diagrams discussed in this chapter represent pairwise Granger-causal relationships with respect to either the complete process in the case of multivariate path diagrams or with respect to bivariate subprocesses in the case of path diagrams depicting bivariate connectivity structures. The results in this section show that both types of path diagrams more generally provide sufficient conditions for Granger-causal relationships with respect to subprocesses X_S for arbitrary subsets S of V .

9.4.1 Separation in graphs and the global Markov property

The basic idea of graphical modelling is to represent the Markov properties of a set of random variables in a graph by relating certain separation properties of the graph to statements about conditional independence or, in the linear case, partial non-correlation between the variables. To this end, we firstly review a path-oriented concept of separating subsets of vertices in a mixed graph that has been used to represent the Markov properties of linear structural equation systems (e.g., [43, 44]). Following Richardson [45] we will call this notion of separation in mixed graphs *m*-separation.

Let $G = (V, E)$ be a mixed graph with directed edges \longrightarrow and undirected edges $---$. A *path* in G is a sequence $\pi = \langle e_1, \dots, e_n \rangle$ of edges $e_i \in E$ with an associated sequence of vertices v_0, \dots, v_n such that edge e_i connects vertices v_{i-1} and v_i . We say that v_0 and v_n are the *endpoints* of the path, while the vertices v_1, \dots, v_{n-1} are the *intermediate vertices* on the path. Note that the vertices v_i in the sequence do not need to be distinct and that therefore the paths considered in this chapter may be self-intersecting.

Furthermore, an intermediate vertex c on a path π is said to be a *collider* on the path if the edges preceding and succeeding c on the path both have an arrowhead or a dashed tail at c , i.e. $\longrightarrow c \longleftarrow$, $\longrightarrow c ---$, $--- c \longleftarrow$, $--- c ---$; otherwise the vertex c is said to be a *non-collider* on the path. Next, let S be a subset of V and let i and j be two vertices that are not in S . Then a path π between the vertices i and j is said to be *m-connecting* given the set S if

- (i) every non-collider on the path is not in S and
- (ii) every collider on the path is in S ,

otherwise we say the path is *m-blocked* given S . If all paths between i and j are *m-blocked* given S , then i and j are said to be *m-separated* given S . Similarly, two disjoint subsets I and J are said to be *m-separated* given S if for every pair $i \in I$ and $j \in J$, the vertices i and j are *m-separated* given S .

To illustrate these graph-theoretic concepts, we consider the graph in Figure 9.4. In this graph, vertices 1 and 4 are *m-separated* given $S = \{3\}$. To show this, we have to examine all paths between the two vertices:

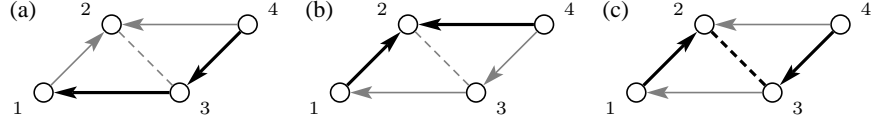


Figure 9.4: Illustration of m -separation in mixed graphs: Vertices 1 and 4 are m -separated given $S = \{3\}$ since all paths between 1 and 4 are m -blocked given S . (a) path $4 \rightarrow 3 \rightarrow 1$ is m -blocked by non-collider $3 \in S$; (b) path $4 \rightarrow 2 \leftarrow 1$ is m -blocked by collider $2 \notin S$; (c) path $4 \rightarrow 3 \text{ --- } 2 \leftarrow 1$ is m -blocked by collider $2 \notin S$.

- We note that every path that passes through vertex 2 contains this vertex as a collider. Two examples of such paths are given in Figure 9.4 (b) and (c). Since 2 is not contained in $S = \{3\}$, all these paths are m -blocked given S .
- The only path between vertices 1 and 4 that does not pass through vertex 2 is the path $4 \rightarrow 3 \rightarrow 1$ (Fig. 9.4(a)). The intermediate vertex 3 on this path is a non-collider and, thus, the path is m -blocked given $\{3\}$.

It follows that there exists no path between 1 and 4 that is m -connecting given $S = \{3\}$, and the vertices 1 and 4 are consequently m -separated given S .

For linear structural equation systems, Koster [44] has shown that the associated path diagrams have indeed a Markov interpretation, namely, if two sets I and J of vertices are m -separated given a third set S , the corresponding variables \mathbf{X}_I and \mathbf{X}_J are independent conditionally on \mathbf{X}_S . The linear equation systems (9.8) for the frequency components $d\mathbf{Z}_{\mathbf{X}_V}(\lambda)$ suggest that a similar result holds also for the frequency components in the time series case. Moreover, since the frequency components at different frequencies are uncorrelated—or independent in the Gaussian case—the separation statements should translate also into non-correlation between complete subprocesses.

To make this precise, let \mathbf{X}_V be a weakly stationary time series with autoregressive representation (9.1), and let G be its associated multivariate path diagram. Furthermore, suppose that I , J , and S are disjoint subsets of V , and let $\mathbf{Y}_{I|S}$ and $\mathbf{Y}_{J|S}$ be the residual time series of \mathbf{X}_I and \mathbf{X}_J , respectively, after the linear effects of the components in \mathbf{X}_S have been removed (see [46], Sect. 8.3). Then the two subprocesses \mathbf{X}_I and \mathbf{X}_J are partially uncorrelated given \mathbf{X}_S if

$$\text{corr}(\mathbf{X}_I(t), \mathbf{X}_J(s) | \mathbf{X}_S) = \text{corr}(\mathbf{Y}_{I|S}(t), \mathbf{Y}_{J|S}(s)) = 0 \quad (9.13)$$

for all $t, s \in \mathbb{Z}$; this will be denoted by $\mathbf{X}_I \perp \mathbf{X}_J | \mathbf{X}_S$. For an alternative formulation in the frequency domain, let

$$\mathbf{f}_{IJ|S}(\lambda) = \mathbf{f}_{IJ}(\lambda) - \mathbf{f}_{IS}(\lambda)\mathbf{f}_{SS}(\lambda)^{-1}\mathbf{f}_{SJ}(\lambda) = \mathbf{f}_{\mathbf{Y}_{I|S}\mathbf{Y}_{J|S}}(\lambda)$$

be the partial cross-spectrum between \mathbf{X}_I and \mathbf{X}_J given \mathbf{X}_S , and let $\mathbf{R}_{IJ|S}(\lambda)$ be the partial spectral coherency given by

$$R_{ij|S}(\lambda) = \frac{f_{ij|S}(\lambda)}{\sqrt{f_{ii|S}(\lambda)f_{jj|S}(\lambda)}} \quad (9.14)$$

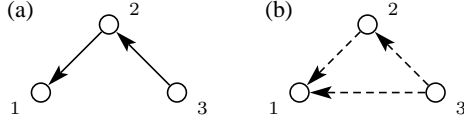


Figure 9.5: (a) Multivariate path diagram associated with the trivariate process \mathbf{X}_V given by (9.16); (b) bivariate path diagram associated with \mathbf{X}_V .

for $i \in I$ and $j \in J$ (see [46], Sect. 8.3). Then condition (9.13) is equivalent to

$$\mathbf{R}_{IJ|S}(\lambda) = 0 \quad \text{for all } \lambda \in [-\pi, \pi]. \quad (9.15)$$

Since the partial spectral coherency can be viewed as the partial correlation between frequency components, this implies that $d\mathbf{Z}_{\mathbf{X}_I}(\lambda)$ and $d\mathbf{Z}_{\mathbf{X}_J}(\lambda)$ are partially uncorrelated given $d\mathbf{Z}_{\mathbf{X}_S}(\lambda)$ for all frequencies $\lambda \in [-\pi, \pi]$. With these definitions, it can be shown (e.g., [19]) that path diagrams associated with vector time series have a Markov interpretation both in the time and the frequency domain.

Theorem 9.4.1. *Suppose \mathbf{X}_V is a weakly stationary time series with autoregressive representation (9.1), and let G be the path diagram associated with \mathbf{X}_V . Furthermore, let I , J , and S be disjoint subsets of V . Then, if I and J are m -separated given S , the process \mathbf{X}_V satisfies*

- (i) $\mathbf{X}_I \perp \mathbf{X}_J \mid \mathbf{X}_S$;
- (ii) $d\mathbf{Z}_{\mathbf{X}_I}(\lambda) \perp d\mathbf{Z}_{\mathbf{X}_J}(\lambda) \mid d\mathbf{Z}_{\mathbf{X}_S}(\lambda)$ for all $\lambda \in [-\pi, \pi]$.

This property is called the global Markov property with respect to G .

As an example, we consider again the four-dimensional process in (9.5) and its associated path diagram in Figure 9.2(a). Here, vertices 1 and 3 are linked by the path $1 \leftarrow 4 \rightarrow 2 \leftarrow 3$. Obviously, the path is m -connecting given S only if $S = \{2\}$ since 2 is a collider and 4 is a non-collider on this path. It follows from Theorem 9.4.1 that the two processes X_1 and X_3 are uncorrelated in a bivariate analysis, but not in a trivariate analysis that includes also X_2 .

9.4.2 The global Granger-causal Markov property

Next, we discuss how the graph-theoretic concepts presented in the previous section can be used for deriving Granger noncausality relations from path diagrams. For a better understanding of the problem, we firstly consider the autoregressive process \mathbf{X}_V given by

$$\begin{aligned} X_1(t) &= \alpha X_2(t-1) + \varepsilon_1(t), \\ X_2(t) &= \beta X_3(t-1) + \varepsilon_2(t), \\ X_3(t) &= \varepsilon_3(t) \end{aligned} \quad (9.16)$$

with $\text{var}(\varepsilon(t)) = \mathbf{I}$. The associated path diagram is shown in Figure 9.5(a). The diagram shows a directed path from vertex 3 to 1, which suggests an indirect causal influence of X_3 on

X_1 . Indeed, noting that the autoregressive representation of the subprocess $\mathbf{X}_{\{1,3\}}$ is given by

$$\begin{aligned} X_1(t) &= \alpha\beta X_3(t-2) + \tilde{\varepsilon}_1(t), \\ X_3(t) &= \tilde{\varepsilon}_3(t) \end{aligned}$$

with $\tilde{\varepsilon}_1(t) = \varepsilon_1(t) + \beta\varepsilon_2(t-1)$, $\tilde{\varepsilon}_3(t) = \varepsilon_3(t)$, and associated bivariate path diagram as shown in Figure 9.5(b), we find that X_3 bivariate Granger-causes X_1 , whereas X_1 is bivariate Granger-noncausal for X_3 . Obviously, the notion of m -separation is too strong for the derivation of such Granger noncausality relations from multivariate path diagrams: the definition of m -separation requires that all paths between vertices 1 and 3 are m -blocked whereas the path $3 \rightarrow 2 \rightarrow 1$ intuitively is interpreted as a causal link from X_3 to X_1 . Consequently, the path should not be considered when discussing Granger noncausality from X_1 to X_3 .

The example suggest the following definition. A path π between vertices j and i is said to be i -pointing if it has an arrowhead at the endpoint i . More generally, a path π between J and I is said to be I -pointing if it is i -pointing for some $i \in I$. In order to establish Granger noncausality from X_J to X_I , it is sufficient to consider only all I -pointing paths between I and J (cf [19]).

Theorem 9.4.2. *Suppose \mathbf{X}_V is a weakly stationary time series with autoregressive representation (9.1) and let G be the path diagram associated with \mathbf{X}_V . Furthermore, suppose that $S \subset V$ and let I and J be two disjoint subsets of S . If every I -pointing path between J and I is m -blocked given $S \setminus J$, then X_J is Granger-noncausal for X_I with respect to X_S .*

Similarly, a graphical condition for contemporaneous correlation can be obtained. Intuitively, two variables X_i and X_j are contemporaneously uncorrelated with respect to X_S if they are contemporaneously uncorrelated with respect to X_V and, furthermore, the variables are not jointly affected by past values of the omitted variables $X_{V \setminus S}$. For a precise formulation of the condition, we need the following definition. A path π between vertices i and j is said to be bi -pointing if it has an arrowhead at both endpoints i and j . Then the sufficient condition for contemporaneous correlation can be stated as follows (cf [19]).

Theorem 9.4.3. *Suppose \mathbf{X}_V is a weakly stationary time series with autoregressive representation (9.1), and let $G = (V, E)$ be the path diagram associated with \mathbf{X}_V . Furthermore, suppose that $S \subset V$ and let I and J be two disjoint subsets of S . If*

- (i) $i \text{ --- } j \notin E$ for all $i \in I$ and $j \in J$, and
- (ii) every bi -pointing path between I and J is m -blocked given S ,

then X_I and X_J are contemporaneously uncorrelated with respect to X_S .

In other words, if two variables X_i and X_j are contemporaneously correlated in the subprocess X_S , then they are also contemporaneously correlated in the full process X_V or the contemporaneous correlation is due to confounding through the variables along an m -connecting path between i and j .

As an example, consider the four-dimensional process \mathbf{X}_V given by (9.5). The path diagram associated with \mathbf{X}_V is shown in Figure 9.6(a). Suppose that we are interested in the Granger-causal relationships that hold for the three-dimensional subprocess $\mathbf{X}_{\{1,2,3\}}$.

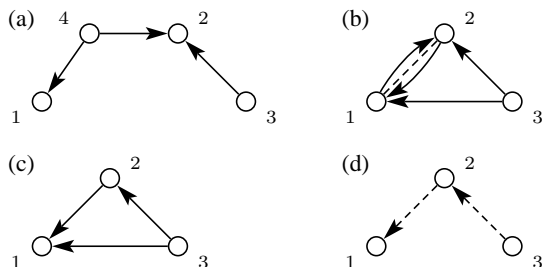


Figure 9.6: (a) Path diagram of four-dimensional process \mathbf{X}_V ; (b) derived path diagram of $\mathbf{X}_{\{1,2,3\}}$ obtained from the graph in (a); (c) path diagram of $\mathbf{X}_{\{1,2,3\}}$; (d) bivariate path diagram of $\mathbf{X}_{\{1,2,3\}}$.

- The directed edge $3 \rightarrow 2$ implies that X_3 Granger-causes X_2 also with respect to $\mathbf{X}_{\{1,2,3\}}$.
- Vertices 1 and 3 are connected by the path $3 \rightarrow 2 \leftarrow 4 \rightarrow 1$. Of the two intermediate vertices 2 and 4 on this path, the former is an m -collider, whereas the latter is an m -non-collider. Thus the path is m -blocked given the set $\{2\}$, which implies by Theorem 9.4.2 that X_3 is Granger-noncausal for X_1 in a bivariate analysis but not in a trivariate analysis including X_2 .
- Vertices 1 and 2 are connected by the bi-pointing path $1 \leftarrow 4 \rightarrow 2$, which is m -blocked only given vertex 4. Therefore, it follows by Theorems 9.4.2 and 9.4.3 that X_1 and X_2 Granger-cause each other and additionally are contemporaneously correlated regardless whether X_3 is included in the analysis or not.

The Granger-causal relationships with respect to $\mathbf{X}_{\{1,2,3\}}$ that can be inferred from the path diagram in Figure 9.6(a) can be summarized by the graph in Figure 9.6(b).

More generally, if a mixed graph G encodes certain Granger noncausality relations of a process \mathbf{X}_V , we say that \mathbf{X}_V satisfies a Markov property with respect to the graph G .

Definition 9.4.4. We say that a weakly stationary time series \mathbf{X}_V satisfies the *global Granger-causal Markov property* with respect to a mixed graph G if for all $S \subseteq V$ and all disjoint subsets I and J of S the following conditions hold:

- (i) \mathbf{X}_J is Granger-noncausal for \mathbf{X}_I with respect to \mathbf{X}_S whenever in the graph G every I -pointing path between J and I is m -blocked given $S \setminus J$.
- (ii) \mathbf{X}_I and \mathbf{X}_J are contemporaneously uncorrelated with respect to \mathbf{X}_S whenever in the graph G the sets I and J are not connected by an undirected edge (---) and every bi-pointing path between I and J is m -blocked given S .

With this definition, Theorems 9.4.2 and 9.4.3 state that a weakly stationary time series \mathbf{X}_V with autoregressive representation (9.1) satisfies the global Granger-causal Markov property with respect to its multivariate path diagram G .

For the four-dimensional vector time series \mathbf{X}_V in (9.5), we have shown above that the Granger-causal relationships with respect to the subprocess $\mathbf{X}_{\{1,2,3\}}$ that can be derived from

the multivariate path diagram (Fig. 9.6(a)) are encoded by the graph in Figure 9.6(b). It follows from Theorems 9.4.2 and 9.4.3 that the trivariate subprocess $\mathbf{X}_{\{1,2,3\}}$ satisfies the global Granger-causal Markov property with respect to the graph in Figure 9.6(b). On the other hand, the autoregressive representation of the subprocess $\mathbf{X}_{\{1,2,3\}}$ is given in (9.6); the corresponding path diagram is depicted in Figure 9.6(c). We note that this path diagram is a subgraph of the graph in Figure 9.6(b), which has been derived from the multivariate path diagram of the complete series \mathbf{X}_V . This demonstrates that Theorems 9.4.2 and 9.4.3 provide only sufficient, not necessary conditions for Granger noncausality with respect to subprocesses.

9.4.3 Markov properties for bivariate path diagrams

Next, we discuss the properties of the bivariate path diagrams introduced in Section 9.3.2. Recall that these path diagrams may have two kind of edges, namely dashed directed edges \dashrightarrow and undirected edges $---$. The representation of bivariate Granger-causal relationships by dashed directed edges allows applying the concept of m -separation without further modifications. More precisely, let G be a mixed graph with directed edges \dashrightarrow and undirected edges $---$ and let π be a path in G . Then the intermediate vertices on π can be characterized as colliders and non-colliders as in the previous section, that is, an intermediate vertex c on the path π is said to be a collider if the edges preceding and succeeding c on the path both have an arrowhead or a dashed tail at c . However, since G contains only edges of the form \dashrightarrow or $---$, it follows that all paths π in G are pure-collider paths, that is, all intermediate vertices are colliders. Consequently, a path π between vertices i and j is m -connecting given a set S if and only if all intermediate vertices are contained in S .

In the previous section, we have shown that the concepts of m -separation and of pointing paths can be used to derive Granger noncausality relations with respect to subprocesses \mathbf{X}_S from multivariate path diagrams. The same is also true for bivariate path diagrams. More precisely, we have the following result (cf [39]):

Theorem 9.4.5. *Let \mathbf{X}_V be a weakly stationary time series with autoregressive representation (9.1) and let G be the bivariate path diagram of \mathbf{X}_V . Then \mathbf{X}_V satisfies the global Granger-causal Markov property with respect to G .*

For an illustration of the Markov interpretation of bivariate path diagrams, we consider again the four-dimensional process \mathbf{X}_V in (9.5) and suppose that variable X_4 has not been observed. The bivariate path diagram associated with the subprocess $\mathbf{X}_{\{1,2,3\}}$ is depicted in Figure 9.6(d); as noted before it can be obtained as subgraph of the bivariate path diagram associated with the complete process \mathbf{X}_V (Fig. 9.3). What can we learn from this diagram about the Granger-causal relationships with respect to $\mathbf{X}_S = \mathbf{X}_{\{1,2,3\}}$?

- Since there is no 3-pointing path in the graph, it follows that the components X_1 and X_2 are Granger-noncausal for X_3 with respect to \mathbf{X}_S . Similarly, the absence of an undirected edge or a bi-pointing path between vertex 3 and the other two vertices implies that $\mathbf{X}_{\{1,2\}}$ and X_3 are contemporaneously uncorrelated with respect to \mathbf{X}_S .
- Vertices 1 and 3 are connected by the 1-pointing path $3 \dashrightarrow 2 \dashrightarrow 1$. This suggests that in a trivariate analysis based on \mathbf{X}_S the series X_3 Granger-causes X_1 .

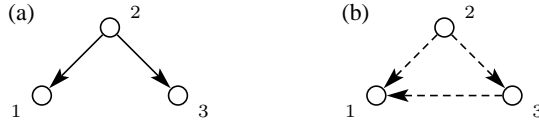


Figure 9.7: (a) Multivariate path diagram associated with the process \mathbf{X}_V in (9.17); (b) bivariate path diagram associated with \mathbf{X}_V .

- Similarly, because of the 2-pointing path $1 \leftarrow 2 \leftarrow 3 \rightarrow 2$, we cannot conclude that X_1 is Granger-noncausal for X_2 with respect to \mathbf{X}_S . Since the path is also bi-pointing, we additionally cannot rule out that X_1 and X_2 are contemporaneously correlated with respect to \mathbf{X}_S .

Summarizing the results, we find that the bivariate path diagram associated with \mathbf{X}_S encodes the same statements about Granger noncausality or contemporaneous non-correlation with respect to \mathbf{X}_S as the graph in Figure 9.6(b).

9.4.4 Comparison of bivariate and multivariate Granger causality

The notion of Granger causality is based on the idea that a correlation between two variables that cannot be explained otherwise must be a causal influence; the temporal ordering then determines the direction of the causal link. This approach requires that all relevant information is included in the analysis. Given data from a multivariate time series \mathbf{X}_V , it therefore seems plausible to discuss Granger causality with respect to the full multivariate process \mathbf{X}_V .

As an example, we consider the vector time series \mathbf{X}_V given by

$$\begin{aligned} X_1(t) &= \alpha X_2(t-2) + \varepsilon_1(t), \\ X_2(t) &= \varepsilon_2(t), \\ X_3(t) &= \beta X_2(t-1) + \varepsilon_3(t), \end{aligned} \tag{9.17}$$

where $\{\varepsilon(t)\}$ is a white noise process with $\text{var}(\varepsilon(t)) = \mathbf{I}$. Simple calculations show that the bivariate path diagram of \mathbf{X}_V is given by the graph in Figure 9.7(b). Here, the bivariate analyses suggest a causal link from X_3 to X_1 although the observed correlation between X_1 and X_3 is only due to confounding by X_2 . In contrast, the multivariate path diagram in Figure 9.7(a) correctly shows neither direct connections nor a causal pathway between X_1 and X_3 . This inability of the bivariate approach to discriminate between causal influences and confounded relationships has been noted by several authors (e.g., [47, 48, 49]).

One serious problem that arises in practice is that relevant variables are omitted from the analysis, for example, because they could not be measured. For an illustration, we consider again the four-dimensional process \mathbf{X}_V in (9.5). As in the previous section, we assume that only the subprocess $\mathbf{X}_S = \mathbf{X}_{\{1,2,3\}}$ is available for an analysis of interrelationships. The multivariate path diagram in Figure 9.6(c) indicates the presence of a direct causal link from X_3 to X_1 , whereas in a bivariate analysis of $\mathbf{X}_{\{1,3\}}$ this Granger-causal influence vanishes. In this situation, the bivariate path diagram in Figure 9.6(d) clearly provides a better graphical description of the relationships among the variables than the multivariate path diagram.

More generally, it can be shown that systems in which all relationships between the observed variables are due to confounding by latent variables can be best represented by bivariate path diagrams. In contrast, multivariate path diagrams are best suited for the representation of causal structures that do not involve confounding by latent variables. In practice, however, causal structures may be a combination of both situations with only a part of the Granger-causal relationships being due to confounding by latent variables. In such cases neither graphical representation would provide an optimal description of the dependencies among the observed variables. Eichler [39] presented a graphical approach for evaluating the connectivity of such systems based on general mixed graphs that generalize both multivariate and bivariate path diagrams.

9.5 Statistical inference

In practice, the autoregressive structure of the processes of interest typically is unknown and must be identified from data. One straightforward approach is to test for the presence of edges in the path diagram; this approach can be used for both types of path diagrams. In the case of multivariate path diagrams, the path diagram can be identified alternatively by model selection based on fitting graphical vector autoregressive models that are constrained according to a path diagram (e.g., [50, 51]).

9.5.1 Inference in the time domain

For the analysis of empirical data, VAR(p) models can be fitted using least squares estimation. For observations $\mathbf{X}_V(1), \dots, \mathbf{X}_V(T)$ from a d -dimensional multiple time series \mathbf{X}_V , let $\hat{\mathbf{R}}_p = (\hat{\mathbf{R}}_p(u, v))_{u, v=1, \dots, p}$ be the $pd \times pd$ matrix composed by submatrices

$$\hat{\mathbf{R}}_p(u, v) = \frac{1}{T-p} \sum_{t=p+1}^T \mathbf{X}(t-u) \mathbf{X}(t-v)'$$

Similarly, we set $\hat{\mathbf{r}}_p = (\hat{\mathbf{r}}_p(0, 1), \dots, \hat{\mathbf{r}}_p(0, p))$. Then the least squares estimates of the autoregressive coefficients are given by

$$\hat{\mathbf{a}}(u) = \sum_{v=1}^p (\hat{\mathbf{R}}_p)^{-1}(u, v) \hat{\mathbf{r}}_p(v) \quad (9.18)$$

for $u = 1, \dots, p$, while the covariance matrix Σ is estimated by

$$\hat{\Sigma} = \frac{1}{T} \sum_{t=p+1}^T \hat{\boldsymbol{\varepsilon}}(t) \hat{\boldsymbol{\varepsilon}}(t)'$$

where $\hat{\boldsymbol{\varepsilon}}(t) = \mathbf{X}(t) - \sum_{u=1}^p \hat{\mathbf{a}}(u) \mathbf{X}(t-u)$ are the least squares residuals. The estimates $\hat{a}_{ij}(u)$ are asymptotically jointly normally distributed with mean $a_{ij}(u)$ and covariances satisfying

$$\lim_{T \rightarrow \infty} T \operatorname{cov}(\hat{a}_{ij}(u), \hat{a}_{kl}(v)) = H_{jl}(u, v) \sigma_{ik},$$

where $H_{jl}(u, v)$ are entries in the inverse $\mathbf{H}_p = \mathbf{R}_p^{-1}$ of the covariance matrix \mathbf{R}_p . For details, we refer to Lütkepohl [52].

The coefficients $a_{ij}(u)$ depend like any regression coefficient on the unit of measurement of X_i and X_j and thus are not suited for comparisons of the strength of causal relationships between different pairs of variables. Therefore, Dahlhaus and Eichler [40] proposed partial directed correlations as a measure of the strength of causal effects. For $u > 0$, the partial directed correlation $\pi_{ij}(u)$ is defined as the correlation between $X_i(t)$ and $X_j(t-u)$ after removing the linear effects of $\mathbf{X}_{V \setminus \{i, j\}}(t-u)$, $u \in \mathbb{N}$. Similarly, we define $\pi_{ij}(0)$ as the correlation between $X_i(t)$ and $X_j(t)$ after removing the linear effects of $\mathbf{X}_V(t-u)$, $u \in \mathbb{N}$, while for $u < 0$ we have $\pi_{ij}(u) = \pi_{ji}(-u)$. It has been shown (see [53]) that estimates for the partial directed correlations $\pi_{ij}(u)$ with $u > 0$ can be obtained from the parameter estimates of a VAR(p) model by rescaling the coefficients $\hat{a}_{ij}(u)$,

$$\hat{\pi}_{ij}(u) = \frac{\hat{a}_{ij}(u)}{\sqrt{\hat{\sigma}_{ii} \hat{\tau}_{ij}(u)}}$$

where

$$\hat{\tau}_{ij}(u) = \hat{K}_{jj} + \sum_{v=1}^{u-1} \sum_{k, l \in V} \hat{a}_{kj}(v) \hat{K}_{kl} \hat{a}_{lj}(v) + \frac{\hat{a}_{ij}(u)^2}{\hat{\sigma}_{ii}}$$

with $\hat{\mathbf{K}} = \hat{\Sigma}^{-1}$. For $u = 0$, we obviously have

$$\hat{\pi}_{ij}(0) = \frac{\hat{\sigma}_{ij}}{\sqrt{\hat{\sigma}_{ii} \hat{\sigma}_{jj}}}.$$

For large sample length T , the partial directed correlations are approximately normally distributed with mean $\pi_{ij}(u)$ and variance $1/T$.

Tests for Granger-causal relationships among the variables can be derived from the asymptotic distribution of the parameters of the VAR(p) model. More precisely, let $\hat{V}(u, v) = \hat{H}_{jj}(u, v) \hat{\sigma}_{ii}$ be the estimate of the asymptotic covariance between $\hat{a}_{ij}(u)$ and $\hat{a}_{ij}(v)$, let $\hat{\mathbf{V}}$ be the corresponding $p \times p$ matrix and set $\hat{\mathbf{W}} = \hat{\mathbf{V}}^{-1}$ with entries $\hat{W}(u, v)$. Then the existence of a Granger-causal effect of X_j on X_i can be tested by evaluating the test statistic

$$S_{ij} = T \sum_{u, v=1}^p \hat{a}_{ij}(u) \hat{W}(u, v) \hat{a}_{ij}(v).$$

Under the null hypothesis that X_j is Granger-noncausal for X_i with respect to \mathbf{X}_V , the test statistic S_{ij} is asymptotically χ^2 distributed with p degrees of freedom.

9.5.2 Inference in the frequency domain

In the frequency domain, the Granger-causal relationships in a multivariate time series \mathbf{X}_V can be evaluated by the Fourier transform

$$\hat{\mathbf{A}}(\lambda) = \sum_{u=1}^p \hat{\mathbf{a}}(u) e^{-i\lambda u},$$

where $\hat{\mathbf{a}}(u)$, $u = 1, \dots, p$, are the autoregressive estimates given by (9.18). From this, estimates for the partial directed coherence can be obtained by suitable normalization. We note that because of the asymptotic normality of the estimates $\hat{a}_{ij}(u)$ the real and imaginary parts of $\hat{A}_{ij}(\lambda)$ are also jointly asymptotically normally distributed. Furthermore, it has been shown (see [54]) that, if $A_{ij}(\lambda) = 0$, then the asymptotic distribution of

$$T \frac{|\hat{A}_{ij}(\lambda)|^2}{C_{ij}(\lambda)}, \quad (9.19)$$

where

$$C_{ij}(\lambda) = \sigma_{ii} \left(\sum_{k,l=1}^p H_{jj}(k,l) [\cos(k\lambda)\cos(l\lambda) + \sin(k\lambda)\sin(l\lambda)] \right), \quad (9.20)$$

is that of a weighted average of two independent χ^2 distributed random variables each with one degree of freedom. Noting that the $1 - \alpha$ quantiles of this asymptotic distribution can be bounded by the $1 - \alpha$ quantile $\chi_{1,1-\alpha}^2$ of a χ^2 distribution with one degree of freedom, we can use

$$\frac{1}{T} \hat{C}_{ij}(\lambda) \chi_{1,1-\alpha}^2,$$

where $\hat{C}_{ij}(\lambda)$ is an estimate of $C_{ij}(\lambda)$ in (9.20), as an approximate α -significance level for testing whether $A_{ij}(\lambda) = 0$. Similarly, a significance level for the partial directed coherence can be derived [54].

We note that the functions $A_{ij}(\lambda)$ like the coefficients $a_{ij}(u)$ depend on the unit of measurement of X_i and X_j and thus are unsuitable for comparing the strength of Granger-causal relationships between different pairs of variables. As noted before, the partial directed coherence does not provide a complete solution to this problem as it measures the relative strength with respect to a given signal source. Instead, we will consider for the examples in Section 9.6 the statistic

$$\hat{\alpha}_{ij}^2(\lambda) = \frac{|\hat{A}_{ij}(\lambda)|^2}{\hat{C}_{ij}(\lambda)},$$

which allows the use of the same significance level $\chi_{1,1-\alpha}^2/T$ for all frequencies λ and all pairs $i, j \in V$. We will call the statistic the *rescaled partial directed coherence* (PDC) from X_j to X_i .

9.5.3 Graphical modelling

An alternative approach for inference on causal structures in multivariate time series is based on fitting graphical vector autoregressive models. For given graph $G = (V, E)$ and order p , we consider vector autoregressive (VAR) models of the form

$$\mathbf{X}_V(t) = \sum_{u=1}^p \mathbf{a}(u) \mathbf{X}_V(t-u) + \boldsymbol{\varepsilon}_V(t), \quad \text{var}(\boldsymbol{\varepsilon}(t)) = \boldsymbol{\Sigma},$$

where the parameters $\mathbf{a}(u)$, $u = 1, \dots, p$, and $\boldsymbol{\Sigma}$ satisfy the constraints

- (i) $a_{ij}(u) = 0$ for $u = 1, \dots, p$ whenever $j \rightarrow i \notin E$ and
- (ii) $\sigma_{ij} = 0$ whenever $i \dashrightarrow j \notin E$.

It follows that the processes \mathbf{X}_V satisfy the global Granger-causal Markov property with respect to the graph G , and we therefore call the VAR model with these constraints on the parameters the graphical vector autoregressive model of order p with respect to graph G or short the VAR(p, G) model.

Given observations $\mathbf{X}_V(1), \dots, \mathbf{X}_V(T)$, the unconstrained parameters in a VAR(p, G) model can be estimated iteratively by the following two steps.

- (i) Let the estimate $\hat{\Sigma}$ be fixed. Then the estimates $\hat{\mathbf{a}}(u)$, $u = 1, \dots, p$ are determined as the solution of the linear equations

$$\left(\sum_{v=1}^p \hat{\Sigma}^{-1} \mathbf{a}(v) \hat{\mathbf{R}}_p(u, v) \right)_{ij} = (\hat{\Sigma}^{-1} \hat{\mathbf{R}}_p(0, v))_{ij}$$

for $u = 1, \dots, p$ and all $i, j \in V$ such that $j \rightarrow i \in E$ under the constraints that $a_{ij}(u) = 0$ whenever the directed edge $j \rightarrow i$ is absent in the graph G .

- (ii) Let $\hat{\mathbf{a}}(u)$, $u = 1, \dots, p$ be fixed and let $\hat{\boldsymbol{\varepsilon}}(t)$ be the corresponding residuals. Then the estimate $\hat{\Sigma}$ is obtained by solving the nonlinear equations

$$(\Sigma^{-1})_{ij} = (\Sigma^{-1} \hat{\Sigma}_0 \Sigma^{-1})_{ij}$$

for all $i, j \in V$ such that $i \dashrightarrow j \in E$, where $\hat{\Sigma}_0 = \frac{1}{T} \sum_{t=p+1}^T \hat{\boldsymbol{\varepsilon}}(t) \hat{\boldsymbol{\varepsilon}}(t)'$ is an unconstrained estimate of Σ .

The second step corresponds to fitting a covariance model to the residuals $\hat{\boldsymbol{\varepsilon}}(t)$, which is determined by the above zero constraints on the covariance matrix Σ . An iterative algorithm for fitting such covariance models has been introduced by Drton and Richardson [55]. Since the solution of both sets of equations are not independent, an iteration of the two steps is needed to obtain a joint solution. For details on fitting graphical vector autoregressive models, we refer to Eichler [53].

Graphical vector autoregressive models can be used to determine the Granger-causal relationships among multiple time series by minimizing model selection criteria like AIC [56] or BIC [57]. The AIC for the VAR(p, G) model is given by

$$\text{AIC}(p, G) = \frac{1}{2} \log |\hat{\Sigma}| + \frac{r}{T},$$

where $\hat{\Sigma}$ is the estimate for Σ in the VAR(p, G) model and r is the number of unconstrained parameters in the model.

9.6 Applications

In this section, we present three examples to demonstrate how graphical representations facilitate our understanding of interrelationships in multivariate time series.

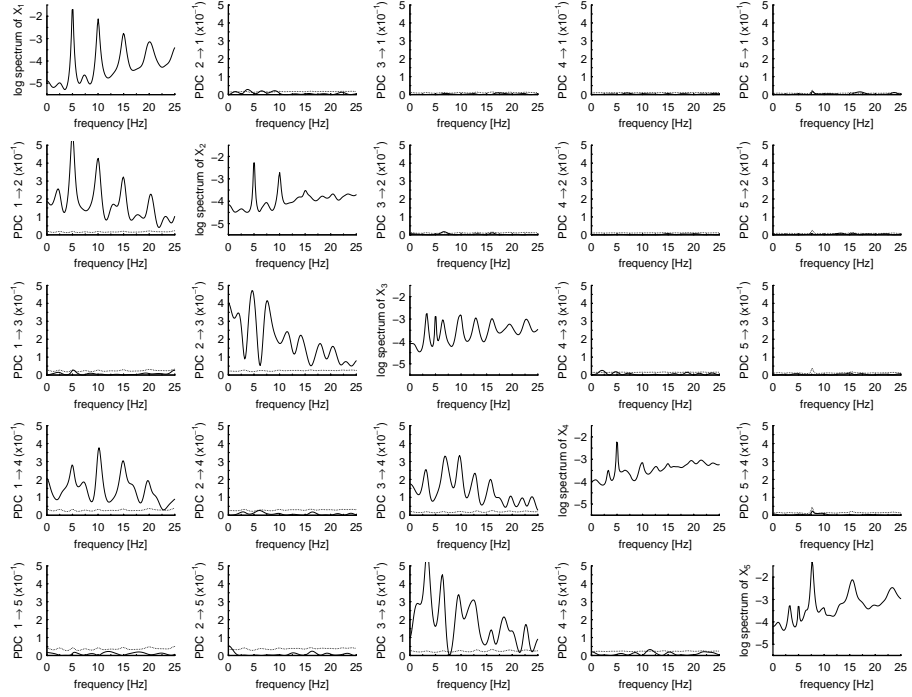


Figure 9.8: Results for neuronal spike train data: estimates of log-spectral densities (*on diagonal*) and non-normalized PDC $|A_{ij}(\lambda)|^2$ (*off-diagonals*). The dotted lines signify pointwise 95% test bounds for the hypothesis that the PDC is zero.

9.6.1 Frequency domain analysis of multivariate time series

In our first example, we review various frequency domain based methods for the description of interrelations among multiple time series and discuss their relations to each other. To illustrate the theoretical results, we apply the methods to neuronal spike train data recorded from the lumbar spinal dorsal horn of a pentobarbital-anaesthetized rat during noxious stimulation. The firing times of ten neurons were recorded simultaneously by a single electrode with an observation time of 100 s. The data have been described in detail in Sandkühler and Eblen-Zajjur [58]; the connectivity among the recorded neurons has been analysed previously by partial correlation analysis [59] and partial directed correlations [60].

For the analysis, we converted the spike trains of five neurons to binary time series and fitted a VAR model of order $p = 100$. Figure 9.8 displays the estimated spectra for these five neurons. The strong peaks in the spectra for neurons 1 and 2 indicate that these neurons show rhythmic discharges at 5 Hz; similarly, neuron 5 fires rhythmically at 7.5 Hz.

For the identification of the effective connectivity among these five neurons, we have estimated the non-normalized PDC $|A_{ij}(\lambda)|^2$ (Fig. 9.8). The PDC detects strongly significant directed relationships for five pairs of neurons. Additionally, tests for contemporaneous non-correlation yielded no significant links between the neurons. Thus, the dependencies between

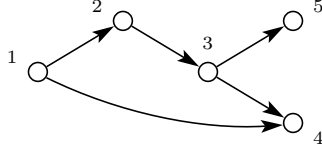


Figure 9.9: Results for neuronal spike train data: Multivariate path diagram identified from the PDCs in Figure 9.8.

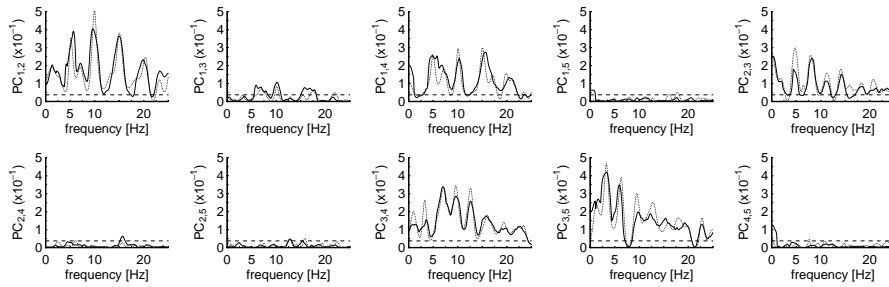


Figure 9.10: Nonparametric (*solid lines*) and parametric (*dotted lines*) estimates of partial spectral coherence for the neuronal spike train data. For the nonparametric estimates, the horizontal dashed lines signify pointwise 95% test bounds for the hypothesis that the partial spectral coherence is zero.

the five neurons can be represented by the path diagram in Figure 9.9.

One non-directional measure for the direct interdependencies between the frequency components of a process \mathbf{X}_V is the *partial spectral coherence* $|R_{ij|V\setminus\{i,j\}}(\lambda)|^2$ with $R_{ij|V\setminus\{i,j\}}(\lambda)$ defined as in (9.14) (see, e.g., [46, 61]). As we have seen in Section 9.4.1, it is closely related to the Markov interpretation of multivariate path diagrams in the frequency domain. In particular, Theorem 9.4.1 implies that the partial spectral coherence $|R_{ij|V\setminus\{i,j\}}(\lambda)|^2$ vanishes uniformly for all frequencies λ whenever the vertices i and j are m -separated given $V\setminus\{i,j\}$.

Figure 9.10 shows nonparametric and parametric estimates of the partial spectral coherence for the neuronal spike train data. Here, the partial spectral coherence between neurons i and j shows a strong association between the corresponding frequency components whenever i and j are connected by an edge. Additionally, we find also a small, but significant partial spectral coherence between neurons 1 and 3, which corresponds with the graphical characterization since in the path diagram in Figure 9.9 vertices 1 and 3 are linked by the m -connecting path $1 \rightarrow 4 \leftarrow 3$.

Another important measure for directed information flow in multivariate systems is the *directed transfer function* (DTF), which has been proposed by Kamiński and Blinowska [62] and is based on the transfer function $\mathbf{B}(\lambda) = (\mathbf{I} - \mathbf{A}(\lambda))^{-1}$. The transfer function relates the frequency components of \mathbf{X} and ε_V by the linear system

$$d\mathbf{Z}_{\mathbf{X}_V}(\lambda) = \mathbf{B}(\lambda) d\mathbf{Z}_{\varepsilon_V}(\lambda)$$

and thus describes how the frequency components of the input process ε_V are transformed by the linear system to the frequency components of the output process X . In particular, the entry $B_{ij}(\lambda)$ measures the response of variable X_i to sinusoidal random shocks of frequency λ at variable X_j . The DTF is a normalized version of the transfer function given by

$$\gamma_{ij}^2(\lambda) = \frac{|B_{ij}(\lambda)|^2}{\sum_k |B_{ik}(\lambda)|^2}. \quad (9.21)$$

and describes the ratio of the influence of component X_j on component X_i to all the influences on component X_i . Due to the normalization, the DTF takes values in $[0, 1]$. For the comparison of the information flow for different target processes or between different experiments, also a non-normalized version of the DTF given by

$$\theta_{ij}^2(\lambda) = |B_{ij}(\lambda)|^2 \quad (9.22)$$

has been suggested [35, 49]. Expanding the inverse $(\mathbf{I} - \mathbf{A}(\lambda))^{-1}$ as a geometric series, we find that

$$B_{ij}(\lambda) = A_{ij}(\lambda) + \sum_{k=1}^d A_{ik}(\lambda) A_{kj}(\lambda) + \sum_{k_1, k_2=1}^d A_{ik_1}(\lambda) A_{k_1 k_2}(\lambda) A_{k_2 j}(\lambda) + \dots \quad (9.23)$$

It follows that the DTF accumulates the information flow from direct pathways—measured by $A_{ij}(\lambda)$ —as well as from indirect pathways via components X_{k_1}, \dots, X_{k_r} . In particular, this implies that the DTF from X_j to X_i vanishes uniformly for all frequencies whenever there exists no directed path $j \rightarrow \dots \rightarrow i$ in the multivariate path diagram associated with \mathbf{X}_V . To illustrate this fact, we estimated the DTF for the neuronal spike train data (Fig. 9.11) with pointwise significance levels as described in Eichler [63]. Comparing the results with the path diagram in Figure 9.9, we find that the DTF indeed identifies information flow from neuron j to neuron i whenever there is a directed path from j to i in the path diagram, which is in line with the graph theoretical predictions.

We conclude that the DTF can be used to describe the propagation of information in multivariate systems, but cannot be used for the detection of the pathways by which the information is propagated, which would entail discrimination between direct and indirect interactions. This also implies that the DTF cannot be used as a measure for Granger causality as defined in Definition 9.2.1 (see [63]).

To resolve the problem of indirect information flow, Korzeniewska et al. [64] proposed a modification of the DTF, which combines the DTF and the partial spectral coherence. This *direct DTF* (dDTF) is defined as the product

$$\delta_{ij}(\lambda) = \gamma_{ij}(\lambda) |R_{ij|V \setminus \{i,j\}}(\lambda)|.$$

The motivation behind this definition is that the DTF $\gamma_{ij}(\lambda)$ measures the propagation of information within a system and, in particular, identifies the direction of the information flow—both direct and indirect—while the partial spectral coherence vanishes if there is no direct interaction between the corresponding frequency components [65]. From the graphical conditions for the partial spectral coherence and the DTF, we immediately find that the dDTF $\delta_{ij}(\lambda)$ vanishes at all frequencies λ whenever in the path diagram

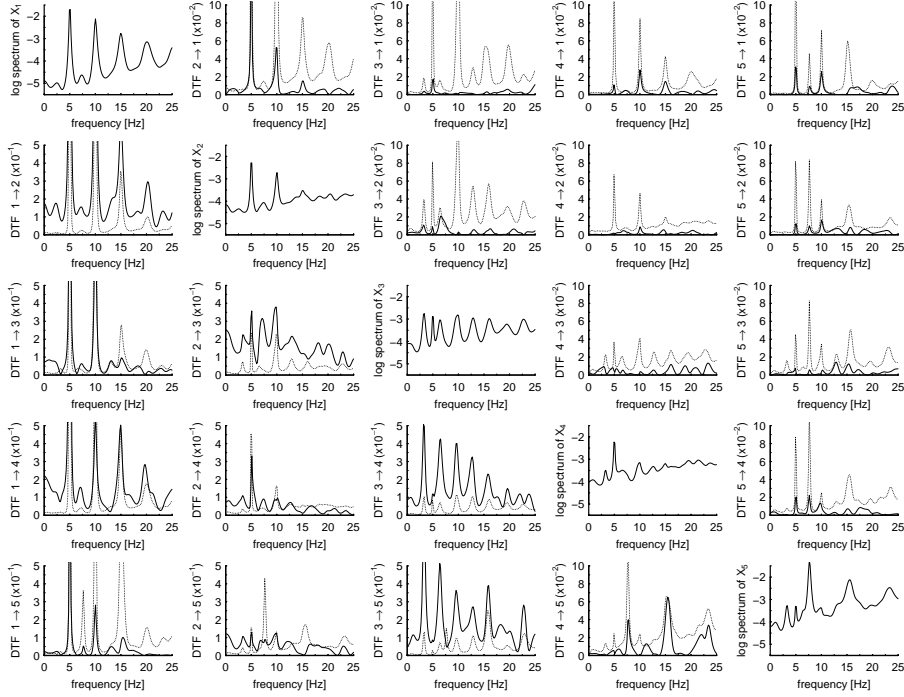


Figure 9.11: Estimates of log-spectral densities (*on diagonal*) and normalized DTF $\gamma_{ij}^2(\lambda)$ (*off-diagonals*) for the neuronal spike train data. The dotted lines signify pointwise 95% test bounds for the hypothesis that the DTF is zero.

- i and j are m -separated given $V \setminus \{i, j\}$ or
- there exists no directed path $j \longrightarrow \dots \longrightarrow i$.

Since the second condition determines only if there is information flow from j to i , the discrimination of direct and indirect information flow must be accomplished by the first condition. This, however, is obviously not the case since two vertices i and j are not m -separated given all other vertices $V \setminus \{i, j\}$ if and only if

- (i) they are linked by an edge (regardless of its direction or type) or
- (ii) connected by a path of the form $i \longrightarrow k \longleftarrow j$.

In particular, this implies that the discrimination fails whenever the path diagram contains a directed cycle, that is, a path of the form $v \longrightarrow \dots \longrightarrow v$. As an example, we consider the path diagram in Figure 9.12(a): in this graph, any two vertices i and j are connected by a directed path from j to i (either $j \longrightarrow i$ or $j \longrightarrow k \longrightarrow i$) and are linked by an edge (either $j \longrightarrow i$ or $i \longrightarrow j$), which means that the dDTF $\delta_{ij}(\lambda)$ is nonzero for all i and j . Clearly, in this case, the dDTF cannot distinguish between direct and indirect information flow (Fig. 9.12(b)).

The effect in (ii) that two independent variables become conditionally dependent if they both affect a third variable that is included in the conditioning set is well known in graphical

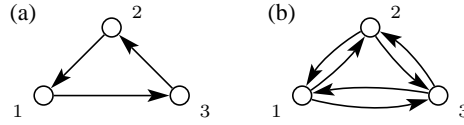


Figure 9.12: (a) Path diagram with one cycle; (b) direct information flow as identified by the dDTF.

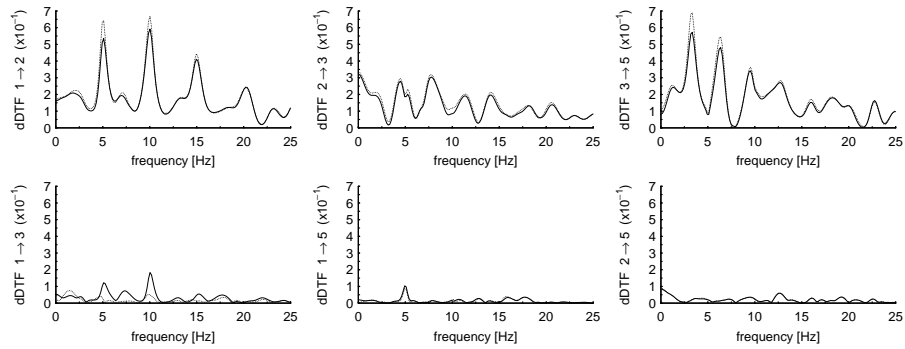


Figure 9.13: Direct DTF (dDTF) for the neuronal spike train data: dDTF obtained from five-dimensional process $X_{\{1, \dots, 5\}}$ (solid lines) and dDTF obtained from four-dimensional process $X_{\{1, 2, 3, 5\}}$ (dotted lines).

modelling theory and is called ‘marrying parents’ effect (see, e.g., [7, 66]). For an illustration of this effect and how it affects the dDTF, we consider again the neuronal spike train data. In the path diagram in Figure 9.9 showing the identified connectivity for the five neurons, we find that the two vertices 1 and 3 are linked by both a directed path ($1 \rightarrow 2 \rightarrow 3$) and an m -connecting path ($1 \rightarrow 4 \leftarrow 3$). According to the above characterization, this implies that the dDTF from X_1 to X_3 is nonzero, and indeed the estimates in Figure 9.13 show two small peaks at frequencies 5 Hz and 10 Hz in the dDTF from neuron 1 to neuron 3. The assessment of the significance of these peaks is difficult since the statistical properties of the dDTF have not been investigated so far. However, we note that the path $1 \rightarrow 4 \leftarrow 3$ is only m -connecting if vertex 4 is included in the separating set. In other words, if neuron 4 is omitted from the analysis, the dDTF should become zero. The corresponding estimates of the dDTF obtained from the process $X_{\{1, 2, 3, 5\}}$ are also shown in Figure 9.13 (dotted curves). Comparing these estimates with those obtained from the full process, we find that the dDTF from neuron 1 to neuron 3 is reduced considerably, while for all other pairs the omission of neuron 4 leaves the estimates basically unchanged. This indicates that the peaks in the former estimate of the dDTF from neuron 1 to neuron 3 were indeed induced by the combination of an m -connecting and a directed pathway from X_1 to X_3 .

If the true path diagram is a directed acyclic graph, that is, it does not contain any undirected edges or directed cycles, then the iterative algorithm presented in Dahlhaus et al. [66] can be applied to identify direct information flow among the components of X_V by the dDTF.

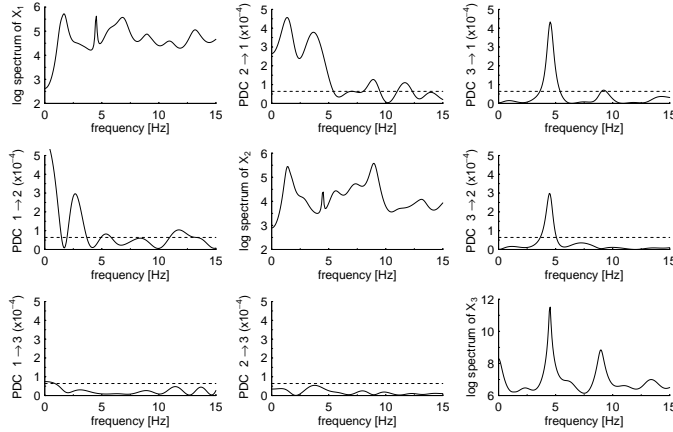


Figure 9.14: Results for tremor-related EEG channels C4 (X_1) and PZA (X_2) and EMG channel (X_3): estimates of log-spectral densities (*on diagonal*) and rescaled PDC $\alpha_{ij}^2(\lambda)$ (*off-diagonals*). The horizontal dashed lines signify pointwise 95% test bounds for the hypothesis that the PDC is zero.

However, in general, identification based on the dDTF can lead to wrongly detected relationships. Therefore, analysis of the information flow and the connectivity in multivariate systems should be based on the PDC or the DTF, which both have a clear interpretation as direct and as total information flow, respectively.

9.6.2 Identification of tremor-related pathways

The second example is concerned with the the analysis of simultaneous electroencephalographic (EEG) and electromyographic (EMG) recordings from patients suffering from essential tremor. This neurological disease manifests itself by an involuntary, oscillatory movement of parts of the body, mainly the upper limbs, with a typical trembling frequency of 4-10 Hz. In previous studies based on coherence analysis, tremor correlated cortical activity has been observed in the EEG [67, 68], but the direction of the relationship remained unclear.

The analysed data consists of the EMG from the left wrist extensor measuring the movement of that hand and the recordings from EEG channels C4 and PZA, which both showed a strong correlation with the EMG at the tremor frequency of about 5 Hz. The EMG signal was band-pass filtered to avoid aliasing effects and undesired slow drifts. Additionally, the signal was digitally full wave rectified. The resulting time series reflects the muscle activity encoded in the envelope of the originally measured signal.

Figure 9.14 shows estimates of the log-spectral densities and the PDC for the data. Furthermore, Table 9.1 shows the significant contemporaneous correlations between the series. This leads to the path diagram in Figure 9.15(a). We note that the EMG signal Granger-causes the EEG signals of both channels C4 and PZA, which suggests that the muscle activity is reflected in the cortex via proprioceptive afferences. Additionally, we find a significant contemporaneous correlation between the EMG signal and channel C4. Since we cannot identify

Table 9.1: p-values for testing for contemporaneous non-correlation in the tremor-related EEG/EMG signals.

C4---PZA	C4---EMG	PZA---EMG
0.000	0.011	0.103

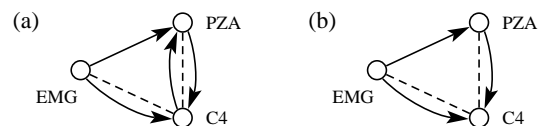


Figure 9.15: Path diagrams for tremor-related EEG/EMG data: (a) path diagram for dependencies over frequency range 0-25 Hz; (a) path diagram for dependencies at tremor frequency $\lambda \approx 5$ Hz.

a direction for this association, it remains an open question whether the oscillatory cortical activity reflected in the signal in channel C4 is involved in the generation of the tremor.

Alternatively, we could restrict ourselves to the dependencies at the tremor frequency, which leads to the omission of the edge $C4 \rightarrow PZA$ (Fig. 9.15(b)). The conclusions concerning the relationship between the EMG signal and the cortical activity, however, remain the same.

9.6.3 Causal inference

In the last example, we apply the graphical approach to concurrent recordings from EEG and functional magnetic resonance imaging (fMRI) for the investigation of the interrelations between the alpha rhythm in the EEG and blood oxygenation level dependent (BOLD) responses in the fMRI. The data and their requisition are described in detail in Goldman et al. [69].

The EEG was sampled at 200 Hz from an array of 16 bipolar pairs, with an additional channel for the EKG and scan trigger. For the analysis, the time-varying spectrum of the EEG has been decomposed by parallel factor (PARAFAC) analysis into trilinear components (called atoms), each being the product of a spatial, spectral, and temporal factors [70]. The PARAFAC analysis extracted three significant atoms characterized by their spectral signature. Only the temporal factor of the alpha atom corresponding to a frequency range 8-12 Hz was included in the effective connectivity analysis.

The fMRI series were measured with a time resolution of 2.5 seconds. Here, we consider two time series of length $T=108$ for two regions in the brain, namely visual cortex and thalamus, whose activation seemed directly related with the EEG alpha atom, namely visual cortex and thalamus. For each region, the time series was obtained by averaging the time series of all voxels in that region.

For the analysis of the effective connectivity, we have fitted a VAR model of order 2 to the data; the order has been determined by minimizing the AIC. Figure 9.16 shows the estimates of the PDC obtained by a trivariate analysis (*solid lines*) and by bivariate analyses (*dotted lines*). Additionally we have tested for contemporaneous non-correlation; the results are given

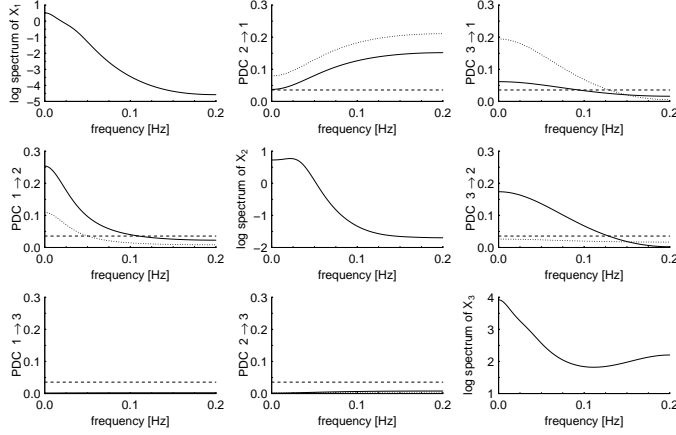


Figure 9.16: Results for fMRI time series from visual cortex (X_1) and thalamus (X_2) and EEG alpha atom (X_3): estimates of log-spectral densities (*on diagonal*) and rescaled PDC $\alpha_{ij}^2(\lambda)$ (*off-diagonals*). The dotted lines represent the rescaled PDCs obtained from bivariate analysis of the corresponding pairs X_i and X_j . The horizontal dashed lines signify pointwise 95% test bounds for the hypothesis that the PDC is zero.

Table 9.2: p-values for testing for multivariate and bivariate contemporaneous non-correlation in the fMRI/EEG data.

	VC --- TH	VC --- EEG	TH --- EEG
bivariate	0.08	0.70	0.22
multivariate	0.00	0.49	0.10

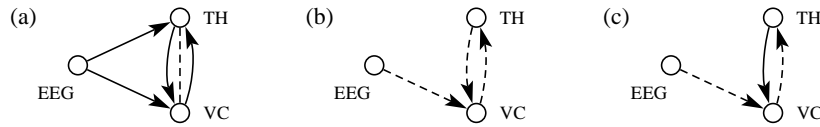


Figure 9.17: Identification of effective connectivity between the EEG alpha atom, the visual cortex, and the thalamus: (a) multivariate path diagram; (b) bivariate path diagram; (c) alternative path diagram that is Markov equivalent to the graph in (b).

in Table 9.2. The results of the analyses are summarized by the multivariate and bivariate path diagrams $G^{(m)}$ and $G^{(b)}$ in Figure 9.17 (a) and (b), respectively. Here, the multivariate path diagram $G^{(m)}$ implies that thalamus and visual cortex neither Granger-cause the EEG alpha atom nor are they contemporaneously correlated with the EEG component, while the bivariate path diagram $G^{(b)}$ additionally encodes that, firstly, the EEG alpha atom does not bivariately Granger-cause the thalamus and, secondly, visual cortex and thalamus are bivariately contemporaneously uncorrelated. Thus the bivariate Granger causality graph encodes more Granger

noncausality relations than the multivariate path diagram, which suggests that at least part of the directed relationships shown in the latter are induced by latent variables.

To describe systems that are partly affected by latent variables, Eichler [39] considered more general graphical representations that combine features of bivariate and multivariate path diagrams. In these graphs, ordinary directed edges (\longrightarrow) represent causal links while dashed directed edges (\dashrightarrow) indicate spurious causalities induced by latent variables. An example of such a graph is shown in Figure 9.17(c). In contrast to $G^{(b)}$, this graph indicates a causal influence from the thalamus to the visual cortex. Simple evaluations show that the graph is Markov equivalent to the bivariate path diagram, that is, it encodes the same relationships among the variables. This implies that we cannot decide empirically between the two graphs as possible descriptions of the connectivity among the variables. We note that in both graphs the correlation between EEG alpha atom and thalamic BOLD responses that is observed in a multivariate analysis is attributed to the indirect link $\text{EEG} \dashrightarrow \text{VC} \dashrightarrow \text{TH}$ mediated by the visual cortex. This is in line with the previous results [70], which identified the visual cortex as the source of the “EEG alpha rhythm”. Similarly, we note that the contemporaneous correlation between thalamus and visual cortex in a multivariate analysis is attributed to the pathway $\text{TH} \leftarrow \text{VC} \leftarrow \text{EEG} \dashrightarrow \text{VC}$.

9.7 Conclusion

In this chapter, we have described a graphical approach for visualizing and analysing the causal relationships in multivariate time series based on the concept of Granger causality. We have seen that by the global (Granger-causal) Markov property certain pathways in a graph can be related to dependencies between the variables. This can be exploited for determining whether a given causal structure that possibly contains unmeasured latent variables is consistent with the dynamic dependencies that have been found empirically between the observed variables. The graphical analysis shows in particular that the causal structure of systems that may be affected by latent variables in general cannot be resolved by multivariate and bivariate analyses alone, but only by examination of Granger noncausality relations with respect to all possible subseries.

In Section 9.6.3, we have briefly touched general Granger causality graphs for the representation of causal structures with latent variables. Unlike bivariate or multivariate path diagrams, which can be specified by pairwise Granger causality relations, these graphs are determined solely through the global Granger-causal Markov property. This holds a number of problems for the empirical identification of causal structures. First, such general Granger causality graphs are not uniquely determined by the Granger noncausality relations that they encode; Figure 9.17 has shown an example of two such Markov equivalent graphs. Secondly, the identification of such graphical representations is based on a multi-step procedure where each step requires the fitting of a new autoregressive model to a subseries. As a consequence, it is impossible to compare two graphical representations of the effective connectivity and to test between them. Moreover, the statistical errors in different steps may lead to contradictory results. To avoid these problems associated with this multi-step identification, future research aims at the development of new graphical time series models that satisfy the global Granger-causal Markov property with respect to such general Granger causality graphs; the

identification of the causal structure could then be achieved by model selection.

Acknowledgements

The data on essential tremor in Section 9.6.2 were recorded by B. Hellwig and B. Guschlbauer at the Department of Neurology of the University of Freiburg, and the EEG-fMRI experiments discussed in Section 9.6.3 were conducted by Robin Goldman and Mark Cohen, which is gratefully acknowledged. Furthermore, the author wishes to thank Pedro Valdéz-Sosa and Eduardo Martínez Montes for many helpful comments on the EEG-fMRI data set.

References

- [1] B. Schack, P. Rappelsberger, S. Weiss, and E. Möller, *Journal of Neuroscience Methods* 93, 49 (1999).
- [2] H. Liang, M. Ding, R. Nakamura, and S.L. Bressler, *NeuroReport* 11, 2875 (2000).
- [3] C.W.J. Granger, *Econometrica* 37, 424 (1969).
- [4] C. Hsiao, *Journal of Economic Dynamics and Control* 4, 243 (1982).
- [5] S. Wright, *Journal of Agricultural Research* 20, 557 (1921).
- [6] S. Wright, *Annals of Mathematical Statistics* 5, 161 (1934).
- [7] J. Whittaker, *Graphical Models in Applied Multivariate Statistics* (John Wiley, Chichester, 1990).
- [8] D.R. Cox and N. Wermuth, *Multivariate Dependencies - Models, Analysis and Interpretation* (Chapman & Hall, London, 1996).
- [9] S.L. Lauritzen, *Graphical Models* (Oxford University Press, Oxford, 1996).
- [10] D. Edwards, *Introduction to Graphical Modelling* (Springer, New York, 2000), 2nd ed.
- [11] J. Pearl, *Artificial Intelligence* 29, 241 (1986).
- [12] J. Pearl, *Probabilistic Inference in Intelligent Systems* (Morgan Kaufmann, San Mateo, California, 1988).
- [13] J. Pearl, *Biometrika* 82, 669 (1995).
- [14] J. Pearl, *Causality* (Cambridge University Press, Cambridge, UK, 2000).
- [15] P. Spirtes, C. Glymour, and R. Scheines, *Causation, Prediction, and Search* (MIT Press, Cambridge, MA, 2001), 2nd ed., With additional material by David Heckerman, Christopher Meek, Gregory F. Cooper and Thomas Richardson.
- [16] S.L. Lauritzen, in *Complex stochastic systems*, edited by O.E. Barndorff-Nielsen, D.R. Cox, and C. Klüppelberg (CRC Press, London, 2001), pp. 63–107.
- [17] M. Eichler, Ph.D. thesis, Universität Heidelberg (1999).
- [18] M. Eichler, Tech. rep., Universität Heidelberg (2001).
- [19] M. Eichler, To appear in *Journal of Econometrics* (2002).
- [20] C.A. Sims, *Econometrica* 48, 1 (1980).

- [21] H.Y. Toda and P.C.B. Philipps, *Econometrica* 61, 1367 (1993).
- [22] B. Hayo, *Applied Economics* 31, 1489 (1999).
- [23] J.F. Geweke, *Journal of the American Statistical Association* 79, 907 (1984).
- [24] P.J. Brockwell and R.A. Davis, *Time Series: Theory and Methods* (Springer, New York, 1991), 2nd ed.
- [25] K. Sameshima and L.A. Baccalá, *Journal of Neuroscience Methods* 94, 93 (1999).
- [26] L.A. Baccalá and K. Sameshima, *Biological Cybernetics* 84, 463 (2001).
- [27] T. Haavelmo, *Econometrica* 11, 1 (1943).
- [28] A.S. Goldberger, *Econometrica* 40, 979 (1972).
- [29] K.A. Bollen, *Structural Equations with Latent Variables* (Wiley, New York, 1989).
- [30] C.W.J. Granger, *Journal of Economic Dynamics and Control* 2, 329 (1980).
- [31] J.P. Florens and M. Mouchart, *Econometrica* 53, 157 (1985).
- [32] Y. Hosoya, *Econometrica* 45, 1735 (1977).
- [33] D. Tjøstheim, *Journal of Econometrics* 17, 157 (1981).
- [34] J.F. Geweke, *Journal of the American Statistical Association* 77, 304 (1982).
- [35] M. Kamiński, M. Ding, W.A. Truccolo, and S.L. Bressler, *Biological Cybernetics* 85, 145 (2001).
- [36] R. Goebel, A. Roebroeck, D.S. Kim, and E. Formisano, *Magnetic Resonance Imaging* 21, 1251 (2003).
- [37] W. Hesse, E. Möller, M. Arnold, and B. Schack, *Journal of Neuroscience Methods* 124, 27 (2003).
- [38] A. Brovelli, M. Ding, L. A. Y. Chen, R. Nakamura, and S.L. Bressler, *Proceedings of the National Academy of Science USA* 101, 9849 (2004).
- [39] M. Eichler, *Philosophical Transactions of The Royal Society B* 360, 953 (2005).
- [40] R. Dahlhaus and M. Eichler, in *Highly structured stochastic systems*, edited by P. Green, N. Hjort, and S. Richardson (University Press, Oxford, 2003).
- [41] C.M. Queen and J.Q. Smith, *Journal of the Royal Statistical Society Series B* 55, 849 (1993).
- [42] M. Reale and G. Tunnicliffe Wilson, *Statistical Methods and Applications* 10, 49 (2001).
- [43] P. Spirtes, T.S. Richardson, C. Meek, R. Scheines, and C. Glymour, *Soc. Methods Res.* 27, 182 (1998).
- [44] J.T.A. Koster, *Scandinavian Journal of Statistics* 26, 413 (1999).
- [45] T. Richardson, *Scandinavian Journal of Statistics* 30, 145 (2003).
- [46] D.R. Brillinger, *Time Series: Data Analysis and Theory* (McGraw Hill, New York, 1981).
- [47] K.J. Blinowska, R. Kuś, and M. Kamiński, *Physical Review E* 70, 050902(R) (2004).
- [48] R. Kuś, M. Kamiński, and K.J. Blinowska, *IEEE Transactions on Biomedical Engineering* 51, 1501 (2004).

- [49] M. Kamiński, *Philosophical Transactions of The Royal Society B* 360, 947 (2005).
- [50] J. Corander and M. Villani, *Journal of Time Series Analysis* 27, 141 (2006).
- [51] M. Eichler (2005), in preparation.
- [52] H. Lütkepohl, *Introduction to Multiple Time Series Analysis* (Springer, New York, 1993).
- [53] M. Eichler (2005), in preparation.
- [54] B. Schelter, M. Winterhalder, M. Eichler, M. Peifer, B. Hellwig, B. Guschlbauer, C.H. Lücking, R. Dahlhaus, and J. Timmer, To appear in *Journal of Neuroscience Methods* (2005).
- [55] M. Drton and T.S. Richardson, Tech. rep., University of Washington (2004).
- [56] H. Akaike, *Annals of the Institute of Statistical Mathematics* 21, 243 (1969).
- [57] G. Schwarz, *Annals of Statistics* 6, 461 (1978).
- [58] J. Sandkühler and A.A. Eblen-Zajjur, *Neuroscience* 61, 991 (1994).
- [59] M. Eichler, R. Dahlhaus, and J. Sandkühler, *Biological Cybernetics* 89, 289 (2003).
- [60] R. Dahlhaus and M. Eichler, in *IFMBE Proceedings EMBEC 2002*, edited by H. Hutten and P. Kroesl (2002), vol. 3(2), pp. 1430–1431.
- [61] J.R. Rosenberg, A.M. Amjad, P. Breeze, D.R. Brillinger, and D.M. Halliday, *Prog. Biophysics Mol. Biol.* 53, 1 (1989).
- [62] M.J. Kamiński and K.J. Blinowska, *Biological Cybernetics* 65, 203 (1991).
- [63] M. Eichler, Tech. rep., University of Heidelberg (2005).
- [64] A. Korzeniewska, M. Maniczak, M. Kaminski, K. Blinowska, and S. Kasicki, *Journal of Neuroscience Methods* 125, 195 (2003).
- [65] R. Dahlhaus, *Metrika* 51, 157 (2000).
- [66] R. Dahlhaus, M. Eichler, and J. Sandkühler, *Journal of Neuroscience Methods* 77, 93 (1997).
- [67] J. Timmer, M. Lauk, B. Köster, B. Hellwig, S. Häußler, B. Guschlbauer, V. Radt, M. Eichler, G. Deuschl, and C.H. Lücking, *International Journal of Bifurcation and Chaos* 10, 2595 (2000).
- [68] B. Hellwig, S. Häußler, B. Schelter, M. Lauk, B. Guschlbauer, J. Timmer, and C.H. Lücking, *Lancet* 357, 519 (2001).
- [69] R.I. Goldman, J.M. Stern, J. Engel, and M.S. Cohen, *NeuroReport* 13, 2487 (2002).
- [70] E. Martínez-Montes, P.A. Valdés-Sosa, F. Miwakeichi, R.I. Goldman, and M.S. Cohen, *NeuroImage* 22, 1023 (2004).